Journal of Computational and Applied Mathematics 473 (2026) 116847

Contents lists available at ScienceDirect

Journal of Computational and Applied Mathematics

journal homepage: www.elsevier.com/locate/cam

Comprehensive closed-form analysis of bifurcation in inductive wireless power transfer systems

Seyit A. Sis

Department of Electrical-Electronics Engineering, Faculty of Engineering, Balikesir University, Cagis, Balikesir, 10145, Turkiye

ARTICLE INFO

Keywords:
Bifurcation
Zero phase angle (ZPA)
Closed-form solution
Inductive wireless power transfer (IWPT)

ABSTRACT

An inductive wireless power transfer (IWPT) system utilizing common compensation topologies-series (SS), series–parallel (SP), parallel–series (PS), and parallel–parallel (PP)-forms a coupled resonant system that exhibits either a single (ω_0) or three zero phase angle (ZPA) frequencies (ω_L, ω_0, and ω_H), depending on the load and coupling conditions. The bifurcation phenomenon in such systems refers to the conditional emergence of two additional ZPA frequencies (ω_L and ω_H) near the inherently present ZPA frequency (ω_0), leading to a total of those three ZPA frequencies. Exact closed-form expressions for the bifurcation criteria, the inherent ZPA frequency (ω_0), as well as the reflected resistance and reactance at ω_0, have been extensively studied and are well-established for all four compensation topologies. However, precise closed-form solutions for these parameters at the conditionally emerging ZPA frequencies (ω_L and ω_H) remain incomplete.

In order to derive the missing closed-form solutions at the ZPA frequencies, this paper reexamines four common compensation topologies in inductive wireless power transfer (IWPT) systems. A circuit model based on mutual inductance is analyzed to establish the necessary equations for the solutions. The primary contribution of this work is to present closed-form expressions for the previously unavailable parameters at ω_L and ω_H. In this context ω_L and ω_H are formulated as functions of the circuit model parameters for all four compensation topologies. Additionally, closed-form expressions for the input resistance (R_{in}) at ω_L and ω_H are derived for all topologies except the PP configuration. The closed-form bifurcation conditions are also presented as function of the circuit parameters for all four topologies. The accuracy of the extracted formulas is validated using an RF circuit simulator.

1. Introduction

Inductive wireless power transfer (IWPT) systems enable the transmission of electrical energy between two objects without physical contact, utilizing electromagnetic induction to transfer power between a transmitter and a receiver coil. This technology has been widely applied in applications such as electric vehicle charging, consumer electronics, and biomedical implants [1,2]. To enhance power transfer efficiency, IWPT systems commonly employ four compensation topologies: series–series (SS), series–parallel (SP), parallel–series (PS), and parallel–parallel (PP) [3–7]. These configurations use capacitors to counteract the inductive reactance of the coils. Depending on the load and coupling conditions, an IWPT system incorporating one of these topologies forms a coupled resonant system with either a single (ω_0) or three $(\omega_L, \omega_0$ and $\omega_H)$ zero phase angle (ZPA) frequencies [7]. ZPA frequencies represent points where the system's input impedance is purely resistive, maximizing power transfer. The phenomenon in which two additional ZPA frequencies, ω_L and ω_H, emerge around ω_0 resulting in a total of three ZPA frequencies is known as bifurcation.

E-mail address: seyit.sis@balikesir.edu.tr.

https://doi.org/10.1016/j.cam.2025.116847
Received 19 February 2025; Received in revised form 21 May 2025
Available online 26 June 2025

Extensive research has already established closed-form expressions for ω_0 and the reflected resistance at ω_0 across all four compensation topologies [7–11]. However, precise closed-form solutions for ω_L, ω_H, and the input resistance (R_{in}) at these frequencies remain incomplete. These solutions are crucial for system design, as operating under these conditions requires thorough analysis. For instance, primary-side controllers and tunable circuits in IWPT systems often rely on tracking ZPA frequencies for various control and optimization purposes [12–21]. Similarly, designing position-independent wireless power transfer systems, utilizing a nonlinear compensation capacitor requires a thorough analysis of ZPA frequencies [22–24].

Several studies [25–33] have investigated bifurcation phenomena and the determination of closed form solutions of and at the ω_L and ω_H. However, many have only provided partial solutions. In [25,26], the analysis was limited to the SS compensation topology and instead of deriving precise values for ω_L and ω_H, only their frequency difference $(\Delta\omega)$ was presented. Moreover, these works did not include closed-form expressions for the input resistance (R_{in}) observed by the inverter at ω_L and ω_H. Studies in [27–31] derived expressions for ω_L and ω_H by differentiating voltage or power gain with respect to frequency, assuming that resonance frequencies align with peak gains. However, this approach may introduce inaccuracies, as peak gain frequencies can deviate from the actual ZPA frequencies. Additionally, these studies focused exclusively on SS topology and did not derive closed-form expressions for R_{in}. In [32], closed-form solutions for ω_L and ω_H were provided, along with exact expressions for R_{in} at these frequencies. However, as with previous works, the analysis was restricted to the SS topology. Meanwhile, [33] identified bifurcation conditions and frequency splitting criteria for constant voltage mode operation in only for the SS-compensation topology, but it did not provide closed-form solutions for ω_L, ω_H and R_{in}. As evident from the literature, many key mathematical expressions related to bifurcation remain unexplored, even for the four fundamental compensation topologies.

This paper aims to address these gaps by deriving exact closed-form solutions for all ZPA frequencies ω_L, ω_0 and ω_H. Furthermore, closed-form expressions for the input resistance (R_{in}) at the conditionally appearing ZPA frequencies $(\omega_\mu$ and $\omega_H)$ are presented for SS, SP, and PS compensation topologies. However, due to the complex nature of the expressions for ω_L and ω_H, the closed-form solution for R_{in} in the PP topology could not be determined. We believe this work significantly advances the mathematical analysis of bifurcation phenomena, building upon the foundational study [7], which originally provided solutions for ω_0.

The remainder of the paper is structured as follows: Section 2 discusses the four compensation topologies and provides a detailed mathematical analysis for each. It also presents the derived ZPA frequencies, bifurcation conditions and R_{in} expressions. Section 3 verifies these solutions using an RF circuit simulator. Finally, Section 4 concludes the study, summarizing the findings and suggesting directions for future research.

2. Bıfurcatıon analysıs of compensatıon topologıes

2.1. SS-compensation topology

A mutual-inductance based circuit model for an IWPT system with an SS compensation topology is shown in Fig. 1. In this model, the L_p and C_p represent coil's self-inductance and compensation capacitance on the primary side. Similarly, the L_s and C_s represent coil's self-inductance and compensation capacitance on the secondary side. Magnetic coupling and the load is represented by mutual inductance (M) and a load resistance (R_L) respectively. The R_L is the resistance seen at the input of the rectifier and basically represents the whole power electronics circuitry and the battery, as a whole, on the receiver side. The Z_{in} is the input impedance seen by the inverter, and is a function of the circuit parameters as follows [7]:

$$Z_{in} = \frac{1}{j\omega C_p} + j\omega L_p + Z_r \tag{1}$$

where Z_r is the reflected impedance taking into account the loading effect of the secondary on the primary circuit and is as follows [7]:

$$Z_r = \frac{\omega^4 C_s^2 M^2 R_L}{\left(\omega^2 C_s L_s - 1\right)^2 + \omega^2 C_s^2 {R_L}^2} - j\frac{\omega^3 C_s M^2 \left(\omega^2 C_s L_s - 1\right)}{\left(\omega^2 C_s L_s - 1\right)^2 + \omega^2 C_S^2 {R_L}^2}. \tag{2}$$

By plugging (2) into (1), Z_{in} can be obtained as follows:

$$Z_{\text{in}} = \frac{C_s^2 M^2 R_L \omega^4}{C_s^2 R_L^2 \omega^2 + \left(-1 + C_s L_s \omega^2\right)^2} + j\left(-\frac{1}{C_p \omega} + L_p \omega - \frac{\omega^3 C_s M^2 \left(\omega^2 C_s L_s - 1\right)}{\left(\omega^2 C_s L_s - 1\right)^2 + \omega^2 C_s^2 R_L^2}\right) \tag{3}$$

The system is operated at secondary the resonant frequency [7] given by

$$\omega_0 = \frac{1}{\sqrt{C_s L_s}} \tag{4}$$

For minimizing input VA rating and achieving maximum power transfer capability, primary side's reactance is also compensated with the primary side capacitance as follows [7]:

$$C_p = \frac{1}{\omega_0^2 L_p}. \tag{5}$$

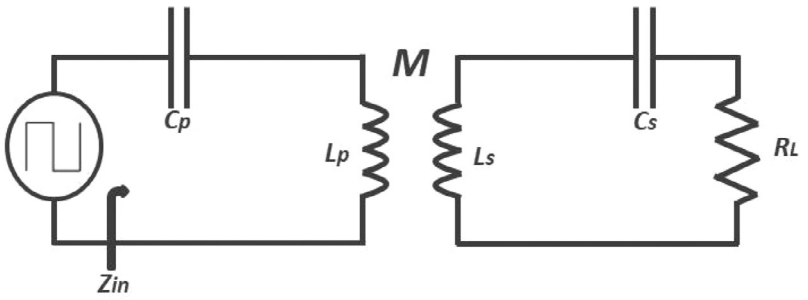

Fig. 1. Schematic of an IWPT system with SS compensation topology.

Table 1
Closed form solutions for ZPA frequencies in SS-compensated IWPT system.

Closed-form solutions for ZPA frequencies	Bifurcation conditions
$\omega_L = \frac{1}{\sqrt{2}}\sqrt{\frac{-2\omega_0^2+C_s^2R_L^2\omega_0^4-\omega_0^3\sqrt{C_s\left(-4C_sR_L^2+4C_pM^2\omega_0^2+C_s^3R_L^4\omega_0^2\right)}}{-1+C_pC_sM^2\omega_0^4}}$	ω_L is real if $\sqrt{C_p}M\omega_0 > \sqrt{C_s}R_L$
$\omega_0 = \frac{1}{\sqrt{C_sL_s}} = \frac{1}{\sqrt{C_pL_p}}$	ω_0 is always real
$\omega_H = \frac{1}{\sqrt{2}}\sqrt{\frac{-2\omega_0^2+C_s^2R_L^2\omega_0^4+\omega_0^3\sqrt{C_s\left(-4C_sR_L^2+4C_pM^2\omega_0^2+C_s^3R_L^4\omega_0^2\right)}}{-1+C_pC_sM^2\omega_0^4}}$	ω_H is real if $\sqrt{C_p}M\omega_0 > \sqrt{C_s}R_L$
Closed-form solutions for Z_{in} at ZPA frequencies	
$Z_{\text{in}}(\omega=\omega_L \text{ or } \omega_H) = R_{\text{in}} = \frac{C_s^2M^2R_L\omega_0^4}{\sqrt{C_s}\omega_0X+C_s^{3/2}(-L_s)\omega_0^3X+C_s(C_pM^2\omega_0^4-2L_s\omega_0^2)+C_s^3L_sR_L^2\omega_0^4+C_s^2(L_s^2\omega_0^4-R_L^2\omega_0^2)+1}$ where $X = \sqrt{\omega_0^2(4C_pM^2+C_s^3R_L^4)-4C_sR_L^2}$	
$Z_{\text{in}}(\omega=\omega_0) = R_{\text{in}} = \frac{M^2\omega_0^2}{R_L}$	

By plugging (4) into (3), ZPA frequencies can be obtained by solving roots of the imaginary part of the Z_{in} $\left(\text{Im}\left(Z_{\text{in}}\right)\right)$ as follows:

$$\text{Im}\left(Z_{in}\right) = \frac{-1+\frac{\omega^2}{\omega_0^2}}{C_p\omega} - \frac{C_SM^2\omega^3\left(-1+\frac{\omega^2}{\omega_0^2}\right)}{C_s^2R_L^2\omega^2+\left(-1+\frac{\omega^2}{\omega_0^2}\right)^2} = 0 \tag{6}$$

One of the solutions of Eq. (6) is ω_0, which is the operating frequency of the system and exists unconditionally as long as the primary side capacitor is chosen according to (5). The Eq. (6) yields two additional real solutions if the following condition, so called bifurcation criteria, is satisfied;

$$\sqrt{C_p}M\omega > \sqrt{C_s}R_L \tag{7}$$

Eq. (6) is solved for ω, yielding three closed-form expressions for the zero-phase angle (ZPA) solutions: ω_L, ω_0 and ω_H, which are presented in Table 1 in ascending order. As shown in Table 1, the solution for ω_0 always exists and remains independent of both mutual inductance (M) and load resistance $\left(R_L\right)$. This ensures that the ZPA frequency ω_0 remains constant regardless of changes in coil orientation or load conditions. In contrast, the other two ZPA frequencies, ω_L and ω_H, exist only when the bifurcation condition is satisfied. These frequencies are highly dependent on all circuit parameters, including M and R_L, causing them to vary with changes in coil alignment and load conditions. The closed-form expressions for the real part of the input impedance $\left(\text{Re}\left(Z_{in}\right)\right)$, known as the input resistance R_{in}, are determined by substituting these ZPA solutions into Eq. (3) and are also listed in Table 1. The impedance values at ω_L and ω_H are equal, resulting in a symmetric impedance profile around Z_{in} at ω_0. The input impedance at ω_0 depends solely on M and R_L, whereas the dependencies at ω_L and ω_H are more complex, as indicated in Table 1.

In certain applications, identical coils are used, leading to equal inductances $(L_s = L_p = L)$ and compensation capacitors $(C_s = C_p = C)$ on both the primary and secondary sides, as inferred from Eqs. (4) and (5). In this case, the expressions in Table 1 are simplified as given in Table 2. As seen in Table 2, when coils are identical and the system meets bifurcation condition $\left(M\omega > R_L\right)$, the R_L is directly reflected to the input of the system at the ω_L and ω_H, with exactly the same value. However, since these frequencies are strongly dependent on M and R_L, operating the system in these frequencies requires implementation of a frequency tracking system [12–14].

Table 2
Closed form solutions for ZPA frequencies in SS-compensated IWPT system with identical coils.

Closed-form solutions for ZPA frequencies for identical coils	Bifurcation conditions
$\omega_L = \frac{1}{\sqrt{2}}\sqrt{\frac{2LC-(CR_L)^2-Cs\sqrt{-4M^2-4CLR_L{}^2+C^2R_L{}^4}}{(LC)^2+C^2M^2}}$	ω_L is real if $M\omega > R_L$
$\omega_0 = \frac{1}{\sqrt{CL}}$	ω_0 is always real
$\omega_H = \frac{1}{\sqrt{2}}\sqrt{\frac{2LC-(CR_L)^2+Cs\sqrt{-4M^2-4CLR_L{}^2+C^2R_L{}^4}}{(LC)^2+C^2M^2}}$	ω_H is real if $M\omega > R_L$
Closed-form solutions for Z_{in} at ZPA frequencies in case of identical coils	
$Z_{\text{in}}\ (\omega = \omega_L \text{ or } \omega_H) = R_{\text{in}} = R_L$	
$Z_{in}\ (\omega = \omega_0) = \frac{M^2\omega_0^2}{R_L}$	

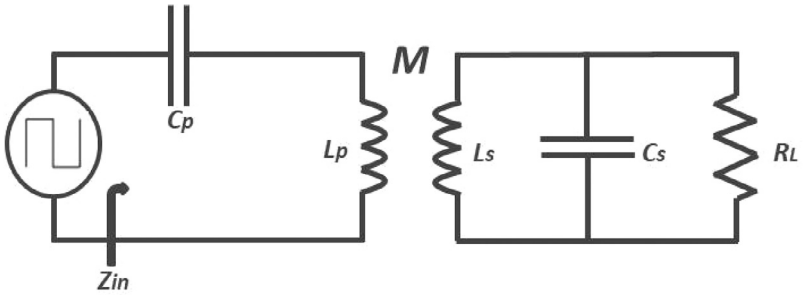

Fig. 2. Schematic of an IWPT system with SP compensation topology.

2.2. SP-compensation topology

The circuit model of the SP-compensated IWPT system is shown in Fig. 2, where the secondary-side capacitor, C_S, is connected in parallel with the secondary-side coil, L_s. The input impedance, Z_{in} , seen by the inverter is a function of the circuit parameters, as given in (1) [7]. The reflected impedance, Z_r, in (1) accounts for the loading effect of the parallel-compensated secondary on the primary circuit and is expressed as follows [7]:

$$Z_r = \frac{\omega^2 M^2 R_L}{R_L^2\left(\omega^2 C_s L_s - 1\right)^2 + \omega^2 L_s^2} - j\frac{\omega^3 M^2\left[C_s R_L^2\left(\omega^2 C_s L_s - 1\right) + L_s\right]}{R_L^2\left(\omega^2 C_s L_s - 1\right)^2 + \omega^2 L_s^2}. \tag{8}$$

By plugging (8) into (1), Z_{in} can be obtained as follows:

$$Z_{\text{in}} = \frac{\omega^2 M^2 R_L}{R_L^2\left(\omega^2 C_s L_s - 1\right)^2 + \omega^2 L_s^2} + i\left(-\frac{1}{C_p\omega} + L_p\omega - \frac{\omega^3 M^2\left[C_s R_L{}^2\left(\omega^2 C_s L_s - 1\right) + L_s\right]}{R_L{}^2\left(\omega^2 C_s L_s - 1\right)^2 + \omega^2 L_s^2}\right). \tag{9}$$

The system operates at the secondary-side resonant frequency [7], as given by (4). To minimize the input VA rating and achieve maximum power transfer, the primary-side reactance is also compensated using the primary-side capacitance, as follows [7]:

$$C_p = \frac{1}{\omega_0^2\left(L_p - M^2/L_s\right)} \tag{10}$$

As seen in (10), C_p is strongly dependent on M, which introduces practical challenges that will be discussed in detail in Section 3. By substituting (10) into (9) and performing a complex expansion, the imaginary part of $\left(Z_{\text{in}}\ \left(\text{Im}\left(Z_{\text{in}}\right)\right)\right.$ can be obtained as follows:

$$\text{Im}\left(Z_{\text{in}}\right) = L_p\omega - \frac{M^2\omega^3\left(L_s + C_s R_L^2\left(-1 + \frac{\omega^2}{\omega_0^2}\right)\right)}{L_s^2\omega^2 + R_L^2\left(-1 + \frac{\omega^2}{\omega_0^2}\right)^2} - \frac{\left(L_p - \frac{M^2}{L_s}\right)\omega_0^2}{\omega} = 0. \tag{11}$$

Eq. (11) is solved for ω, yielding three closed-form expressions for the ZPA solutions $(\omega_L, \omega_0$ and $\omega_H)$, which are provided in Table 3. As shown in Table 3, the real ω_0 solution always exists and is independent of M and R_L, ensuring that this ZPA frequency remains constant regardless of changes in coil orientation or load conditions. The other two real ZPA solutions ($\omega_{\mathcal{L}}$ and ω_H) exist only when the bifurcation condition is met, and their values strongly depend on all circuit parameters, including M and R_L. Table 3 also presents the closed-form expressions for the real part of the input impedance $\left(\text{Re}\left(Z_{\text{in}}\right)\right)$, referred to as the input resistance R_{in}, at all three ZPA frequencies. As seen in Table 3, Z_{in} at ω_0 depends only on M and R_L, whereas its dependence on circuit parameters

Table 3
Closed form solutions for ZPA frequencies in SP-compensated IWPT system.

Closed-form solutions for ZPA frequencies	Bifurcation conditions
$\omega_L = \frac{\sqrt{\frac{\left(2L_pL_s-M^2\right)R_L^2\omega_0^2+Ls^2\left(-L_pL_s+M^2\right)\omega_0^4-\sqrt{\omega_0^4\left(-4L_s\left(L_pL_s-M^2\right)R_L^4\left(L_p-C_sM^2\omega_0^2\right)+\left(\left(-2L_pL_s+M^2\right)R_L^2+Ls^2\left(L_pL_s-M^2\right)\omega_0^2\right)^2\right)}}{L_sR_L^2\left(L_p-C_sM^2\omega_0^2\right)}}}{\sqrt{2}}$	ω_L is real if: $\omega_0^2Ls^3L_p - M^2\omega_0^2Ls^2 < M^2R_L^2$
$\omega_0 = \frac{1}{\sqrt{C_sL_s}}$	ω_0 is always real
$\omega_H = \frac{\sqrt{\frac{\left(2L_pL_s-M^2\right)R_L^2\omega_0^2+Ls^2\left(-L_pL_s+M^2\right)\omega_0^4+\sqrt{\omega_0^4\left(-4L_s\left(L_pL_s-M^2\right)R_L^4\left(L_p-C_sM^2\omega_0^2\right)+\left(\left(-2L_pL_s+M^2\right)R_L^2+Ls^2\left(L_pL_s-M^2\right)\omega_0^2\right)^2\right)}}{L_sR_L^2\left(L_p-C_sM^2\omega_0^2\right)}}}{\sqrt{2}}$	ω_L is real if: $\omega_0^2Ls^3L_p - M^2\omega_0^2Ls^2 < M^2R_L^2$
Closed-form solutions for Z_{in} at ZPA frequencies	
$Z_{\text{in}}\left(\omega=\omega_L\right)=R_{\text{in}} = \frac{M^2\left(\left(2L_pL_s-M^2\right)R_L^2\omega_0^2+Ls^2\left(-L_pL_s+M^2\right)\omega_0^4-y\right)}{2L_sR_L\left(L_p-C_sM^2\omega_0^2\right)\left(-\frac{L_s\left(\left(-2L_pL_s+M^2\right)R_L^2\omega_0^2+Ls^2\left(L_pL_s-M^2\right)\omega_0^4+y\right)}{2R_L^2\left(L_p-C_sM^2\omega_0^2\right)}+\left(R_L+\frac{C_s\left(\left(-2L_pL_s+M^2\right)R_L^2\omega_0^2+Ls^2\left(L_pL_s-M^2\right)\omega_0^4+y\right)}{2R_L\left(L_p-C_sM^2\omega_0^2\right)}\right)^2\right)}$	
$Z_{\text{in}}\left(\omega=\omega_H\right)=R_{\text{in}} = \frac{M^2\left(\left(2L_pL_s-M^2\right)R_L^2\omega_0^2+Ls^2\left(-L_pL_s+M^2\right)\omega_0^4+y\right)}{2L_sR_L\left(L_p-C_sM^2\omega_0^2\right)\left(\frac{L_s\left(\left(2L_pL_s-M^2\right)R_L^2\omega_0^2+Ls^2\left(-L_pL_s+M^2\right)\omega_0^4+y\right)}{2R_L^2\left(L_p-C_sM^2\omega_0^2\right)}+\left(R_L-\frac{C_s\left(\left(2L_pL_s-M^2\right)R_L^2\omega_0^2+Ls^2\left(-L_pL_s+M^2\right)\omega_0^4+y\right)}{2R_L\left(L_p-C_sM^2\omega_0^2\right)}\right)^2\right)}$	
where	
$y=\sqrt{\omega_0^4\left(-4L_s(L_pL_s-M^2)R_L^4(L_p-C_sM^2\omega_0^2)+\left((-2L_pL_s+M^2)R_L^2+Ls^2(L_pL_s-M^2)\omega_0^2\right)^2\right)}$	
$Z_{\text{in}}(\omega=\omega_0)=R_{\text{in}}=\frac{M^2R}{L_s^2}$	

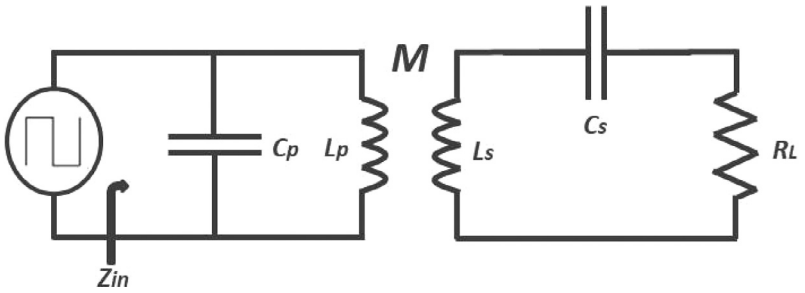

Fig. 3. Schematic of an IWPT system with PS compensation topology.

is more complex at $\omega_{\mathcal{L}}$ and $\omega_{\mathcal{H}}$. When the coils are identical, the expressions in Table 3 can be further simplified; however, unlike in SS-compensation, these simplifications are not as significant. Therefore, separate results for the SPcompensation case are not provided in a different table.

2.3. PS-compensation topology

The circuit model for a PS-compensated IWPT system is shown in Fig. 3. In this model, both secondary side capacitor, C_s and primary side capacitor, C_p, are connected parallel to L_s and L_p, respectively, as shown in Fig. 3. The Z_{in} is the input impedance seen by the inverter, and is a as follows [7]:

$$Z_{in} = \frac{1}{j\omega C_p + \frac{1}{j\omega L_p + Z_r}}. \tag{12}$$

The system operates at the secondary-side resonant frequency [7], as given by (4). To minimize the input VA rating and achieve maximum power transfer, the primary-side reactance is also compensated using the primary-side capacitance, as follows [7]:

$$C_p = \frac{L_p}{\left(\frac{\omega_0^2M^2}{R_L}\right)^2 + \omega_0^2L_p^2} \tag{13}$$

Table 4
Closed form solutions for ZPA frequencies in PS-compensated IWPT system.

Closed-form solutions for ZPA frequencies	Bifurcation conditions
$\omega_L = \frac{1}{\sqrt{2}}\sqrt{-\frac{-2L_p^3R_L^2\omega_0^2+L_p\left(-M^4+C_sL_pM^2R_L^2+C_s^2L_p^2R_L^4\right)\omega_0^4+C_sM^4\left(M^2+C_sL_pR_L^2\right)\omega_0^6+A}{L_pR_L^2\left(L_p-C_sM^2\omega_0^2\right)^2}}$	ω_L is real if Eq. (17) is satisfied
$\omega_0 = \frac{1}{\sqrt{C_sL_s}}$	ω_0 is always real
$\omega_H = \frac{1}{\sqrt{2}}\sqrt{\frac{2L_p^3R_L^2\omega_0^2+L_p\left(M^4-C_sL_pM^2R_L^2-C_s^2L_p^2R_L^4\right)\omega_0^4-C_sM^4\left(M^2+C_sL_pR_L^2\right)\omega_0^6+A}{L_pR_L^2\left(L_p-C_sM^2\omega_0^2\right)^2}}$	ω_L is real if Eq. (17) is satisfied
Closed-form solutions for Z_{in} at ZPA frequencies	
$Z_{\text{in}}\ (\omega=\omega_L) = R_{\text{in}} = \frac{2C_sLp^4R_L{}^4\omega_0^2+L_pM^2\left(M^4+C_sL_pM^2R_L^2-C_S{}^2L_P^2R_L{}^4\right)\omega_0^4-C_sM^6\left(M^2+C_sL_pR_L{}^2\right)\omega_0^6-M^2A}{2C_S{}^2R_L{}^2\omega_0^2\left(L_P{}^2R_L^2+L_pM^4\omega_0^2\right)}$	
$Z_{\text{in}}\ (\omega=\omega_H) = R_{\text{in}} = \frac{2C_sLp^4R_L^4\omega_0^2+L_pM^2\left(M^4+C_sL_pM^2R_L^2-C_S^2L_P^2R_L^4\right)\omega_0^4-C_sM^6\left(M^2+C_sL_pR_L^2\right)\omega_0^6+M^2A}{2C_S{}^2R_L^2\omega_0^2\left(L_P{}^2R_L^2+L_pM^4\omega_0^2\right)}$	
$Z_{\text{in}}\ (\omega=\omega_0) = R_{\text{in}} = \frac{L_P^2R_L}{M^2}+\frac{M^2\omega_0^2}{R_L}$	
where	
$A=\Big[-4L_pR_L^2\left(L_p-C_sM^2\omega_0^2\right)^2\left(L_p^3R_L^2\omega_0^4+L_pM^4\omega_0^6\right)+\left(-2L_p^3R_L^2\omega_0^2+L_p\left(-M^4+C_sL_pM^2R_L^2+C_s^2L_p^2R_L^4\right)\omega_0^4+C_sM^4\left(M^2+C_sL_pR_L^2\right)\omega_0^6\right)^2\Big]^{1/2}$	

As seen in (13), C_p is strongly dependent on both M and R_L, leading to practical challenges that will be discussed in detail in Section 3. In (12), Z_r represents the reflected impedance, which accounts for the loading effect of the secondary on the primary circuit and was previously given in (2) for a series-compensated secondary [7]. By substituting (2) and (13) into (12), the Z_{in}, for a PS-compensation is as follows:

$$Z_{\text{in}} = \frac{1}{\frac{-j\omega^2+(i-C_sR_L\omega)\omega_0^2}{L_p\omega^3-\omega\left(L_p+iC_sL_pR_L\omega+C_sM^2\omega^2\right)\omega_0^2}+\frac{jL_p\omega}{L_p{}^2\omega_0^2+\frac{M^4\omega_0^4}{R_L{}^2}}}. \tag{14}$$

By performing a complex expansion of the expression in (14), the imaginary part of the input impedance is obtained as shown in (15). In (15), the parameters K, T, U and F are defined in (16). Subsequently, the ZPA frequencies can be determined by solving for the roots of the imaginary part of Z_{in}, $\left(\text{Im}\left(Z_{in}\right)\right)$, with the solutions provided in Table 4.

$$\text{Im}\left(Z_{in}\right) = \frac{T\omega\left(L_p^2R_L^2\omega_0^2+M^4\omega_0^4\right)\left(C_sM^6\omega^2\omega_0^6+C_sL_p^2M^2R_L^2\omega^2\omega_0^2\left(-2\omega^2+\omega_0^2\right)+L_p^3R_L^2K+L_pM^4\omega_0^4\left(\omega_0^2+\omega^2\left(-1+C_s^2R_L^2\left(\omega^2+\omega_0^2\right)\right)\right)\right)}{2TC_sL_pM^6R_L^2\omega^4\omega_0^6-2C_sL_p^3M^2R_L^4\omega^4\omega_0^2\left(\omega^2-\omega_0^2\right)^2+L_p^2M^4R_L^2\omega_0^4\left(\omega^6(-2+U)+6\omega^4\omega_0^2-2\omega^2(3+U)\omega_0^4+2(1+U)\omega_0^6\right)+M^8\omega_0^8K+L_p^4R_L^4FK} \tag{15}$$

$$K = \left(\omega^4+\omega_0^4+\omega^2\omega_0^2\left(-2+C_s^2R_L^2\omega_0^2\right)\right) \tag{16a}$$

$$T = (\omega-\omega_0)(\omega+\omega_0) \tag{16b}$$

$$U = C_s^2R_L^2\omega^2 \tag{16c}$$

$$F = (\omega-\omega_0)^2(\omega+\omega_0)^2 \tag{16d}$$

$$\left(-2L_p^3R_L^2\omega_0^2+L_p\left(-M^4+C_sL_pM^2R_L^2+C_s^2L_p^2R_L^4\right)\omega_0^4+C_sM^4\left(M^2+C_sL_pR_L^2\right)\omega_0^6\right)^2 > 4L_pR_L^2\left(L_p-C_sM^2\omega_0^2\right)^2\left(L_p^3R_L^2\omega_0^4+L_pM^4\omega_0^6\right) \tag{17}$$

As seen in Table 4, the real ω_0 solution always exists and is independent of the M and R_L, making this ZPA frequency stays constant even if the coils' orientation to one another and/or the load conditions vary as long as primary side capacitor is tuned according to those variations as given in (13). The other two real ZPA solutions (ω_L and ω_H) exist only when bifurcation condition, as given in (17), is met, and their values are strongly dependent on all circuit parameters including M and R_L. The closed form expressions for the real part of the input impedance $\left(\text{Re}\left(Z_{in}\right)\right)$, namely, the input resistances, R_{in}, at all three ZPA frequencies are

also given in Table 4. As seen in Table 4, the Z_{in} at ω_0 is dependent on only the M, R_L, L_p and ω_0, whereas it is dependency to circuit parameters are more complex at the ω_L and ω_H.

2.4. PP-compensation topology

The circuit model of a parallel-parallel (PP) compensated inductive wireless power transfer (IWPT) system is illustrated in Fig. 4. In this configuration, both the secondary-side capacitor, C_5, and the primaryside capacitor, C_p, are connected parallel to the primary and secondary side inductors L_s and L_p, respectively, as depicted in Fig. 4. Since both sides utilize parallel compensation, the analysis is conducted using admittances to simplify the mathematical expressions. Accordingly, the imaginary component of the input admittance is first derived as follows:

$$Y_{in} = j\omega C_p + \frac{1}{j\omega L_p + Z_r}. \tag{18}$$

In Eq. (18), Z_r represents the reflected impedance, which accounts for the loading effect of the parallel-compensated secondary on the primary circuit. The expression for Z_r was previously provided in Eq. (8) for a parallel-compensated secondary [7]. The system operates at the secondary-side resonant frequency, as defined in Eq. (4) [7]. To minimize the input volt–ampere (VA) rating and achieve maximum power transfer efficiency, the reactance on the primary side is also compensated using the primary-side capacitance, as shown below [7]:

$$C_p = \frac{L_p - M^2/L_s}{\left(\frac{M^2 R_L}{L_s^2}\right)^2 + \omega_0^2 \left(L_p - M^2/L_s\right)^2} \tag{19}$$

By substituting Eqs. (8) and (19) into Eq. (18), the input admittance Y_{in} for a PP-compensated IWPT system is derived in Eq. (20). Expanding the expression in Eq. (20) into its complex components, the real and imaginary parts of the input admittance are obtained in Eqs. (21) and (22), respectively. As observed in Eq. (19), the primary-side capacitance C_p is highly dependent on the mutual inductance M, load resistance R_L, and coil inductances (L_p and L_s), which introduces certain practical challenges.

$$Y_{in} = \frac{iL_s^3\left(L_pL_s - M^2\right)\omega}{M^4R_L^2 + L_s^2\left(-L_pL_s + M^2\right)^2\omega_0^2} - \frac{i}{\omega\left(L_p - \frac{M^2\omega\omega_0^2\left((iR_L - L_s\omega)\omega_0^2 + C_sR_L^2\omega(\omega-\omega_0)(\omega+\omega_0)\right)}{L_s^2\omega^2\omega_0^4 + R_L^2\left(\omega^2-\omega_0^2\right)^2}\right)} \tag{20}$$

$$\begin{aligned} \mathrm{Re}\left(Y_{\mathrm{in}}\right) &= \frac{M^2R_L\omega_0^2}{D_1\left(\frac{M^4R_L^2\omega^2\omega_0^8}{D_1^2} + D_2\right)}, \\ \text{where} \quad D_1 &= L_s^2\omega^2\omega_0^4 + R_L^2(\omega^2-\omega_0^2)^2, \\ D_2 &= L_p - \frac{M^2\omega\omega_0^2\left(L_s\omega\omega_0^2 + C_sR_L^2\omega(\omega^2-\omega_0^2)\right)}{D_1}. \end{aligned} \tag{21}$$

$$\begin{aligned} \mathrm{Im}\left(Y_{in}\right) &= \frac{L_pL_s^4\omega - L_s^3M^2\omega}{M^4R_L^2 + L_s^2\left(-L_pL_s + M^2\right)^2\omega_0^2} \\ &- \frac{L_p}{\omega\left(\frac{M^4R_L^2\omega^2\omega_0^8}{\left(L_s^2\omega^2\omega_0^4 + R_L^2\left(\omega^2-\omega_0^2\right)^2\right)^2} + \left(L_p - \frac{M^2\omega\omega_0^2\left(L_s\omega\omega_0^2 + C_sR_L^2\omega(\omega-\omega_0)(\omega+\omega_0)\right)}{L_s^2\omega^2\omega_0^4 + R_L^2\left(\omega^2-\omega_0^2\right)^2}\right)^2\right)} \\ &+ \frac{C_sM^2R_L^2\omega^3\omega_0^2 + L_sM^2\omega\omega_0^4 + C_sM^2R_L^2\omega\omega_0^4}{\left(L_S^2\omega^2\omega_0^4 + R_L^2\left(\omega^2-\omega_0^2\right)^2\right)\left(\frac{M^4R_L^2\omega^2\omega_0^8}{\left(L_s^2\omega^2\omega_0^4 + R_L^2\left(\omega^2-\omega_0^2\right)^2\right)^2} + \left(L_p - \frac{M^2\omega\omega_0^2\left(L_s\omega\omega_0^2 + C_sR_L^2\omega(\omega-\omega_0)(\omega+\omega_0)\right)}{L_s^2\omega^2\omega_0^4 + R_L^2\left(\omega^2-\omega_0^2\right)^2}\right)^2\right)} \end{aligned} \tag{22}$$

Finally, the ZPA frequencies can be determined by solving for the roots of the imaginary component of the input admittance, $\left(\mathrm{Im}\left(Y_{in}\right)\right)$, with the results summarized in Table 5. As shown in Table 5, the fundamental ZPA frequency ω_0 always exists and remains independent of the mutual inductance M and load resistance R_L. This ensures that ω_0 remains constant regardless of variations in coil alignment or load conditions, provided that the primary-side capacitor is properly tuned according to these changes, as specified in Eq. (19). The other two ZPA frequencies, ω_L and ω_H only exist when the bifurcation condition, given in Eq. (24), is satisfied. Table 5 further demonstrates that ω_L and ω_H are significantly influenced by all circuit parameters, including M and R_L. Due to the complexity of their expressions, the solutions for ω_L and ω_H have been represented using a series of sub-expressions, provided in Eqs. (25)–(36).

The closed form expressions for the real part of the input admittance $\left(\mathrm{Re}\left(\mathrm{Y}_{\mathrm{in}}\right)\right)$, namely, the input conductance, G_{in} , at ω_0, is obtained by plugging the ω_0 into (20) and is reduced to expression in (23). A closed-form expression for G_{in} at ω_L and ω_H could not be derived, as the closed-form solutions for ω_L and ω_H are already too complex to substitute (21). Instead, one can directly use

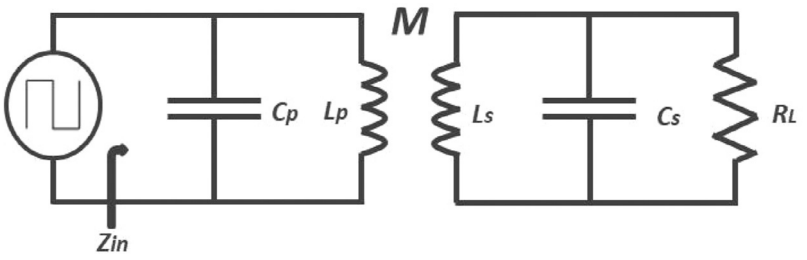

Fig. 4. Schematic of an IWPT system with PP compensation topology.

Table 5
Closed form solutions for ZPA frequencies in PP-compensated IWPT system with identical coils.

Closed-form solutions for ZPA frequencies
$\omega_L = \sqrt{\frac{z}{4L_s^3R_L^2uv}+\frac{1}{2}\sqrt{\frac{b}{3c}+\frac{3g^2p+4sL_s^3u-12bL_s^3pu}{12L_s^6pR_L^4u^2v^2}+\frac{p}{3\left(2^{\frac{1}{3}}\right)L_s^3R_L^4uv^2}}-\frac{1}{2}\sqrt{-\frac{b}{3c}+\frac{-\frac{g^3}{L_s^9R_L^6u^3v^3}+\frac{4bg}{L_s^6R_L^6u^2v^3}-\frac{8t}{L_s^3R_L^6uv^2}}{4\sqrt{\frac{b}{3c}+\frac{3g^2p+4sL_s^3u-12bL_s^3pu}{12L_s^6pR_L^4u^2v^2}+\frac{p}{3\left(2^{1/3}\right)L_s^3R_L^4uv^2}}}+\frac{3g^2p-2sL_s^3u-6bL_s^3pu}{6L_s^6pR_L^4u^2v^2}-\frac{p}{3\left(2^{1/3}\right)L_s^3R_L^4uv^2}}}$
$\omega_0 = \frac{1}{\sqrt{C_sL_s}}$
$\omega_H = \sqrt{\frac{z}{4L_s^3R_L^2uv}+\frac{1}{2}\sqrt{\frac{b}{3c}+\frac{3g^2p+4sL_s^3u-12bL_s^3pu}{12L_s^6pR_L^4u^2v^2}+\frac{p}{3\left(2^{\frac{1}{3}}\right)L_s^3R_L^4uv^2}}+\frac{1}{2}\sqrt{-\frac{b}{3c}+\frac{-\frac{g^3}{L_s^9R_L^6u^3v^3}+\frac{4bg}{L_s^6R_L^6u^2v^3}-\frac{8t}{L_s^3R_L^6uv^2}}{4\sqrt{\frac{b}{3c}+\frac{3g^2p+4sL_s^3u-12bL_s^3pu}{12L_s^6pR_L^4u^2v^2}+\frac{p}{3\left(2^{1/3}\right)L_s^3R_L^4uv^2}}}+\frac{3g^2p-2sL_s^3u-6bL_s^3pu}{6L_s^6pR_L^4u^2v^2}-\frac{p}{3\left(2^{1/3}\right)L_s^3R_L^4uv^2}}}$

the numerical values of ω_L and ω_H in (21) to calculate the numerical value of G_{in} rather than attempting to find its closed-form expression.

$$Y_{in}\left(\omega=\omega_0\right)=G_{in}=\frac{L_s^2M^2R_L}{M^4R_L^2+L_s^2\left(-L_pL_s+M^2\right)^2\omega_0^2} \tag{23}$$

The bifurcation condition for ω_L and ω_H to exhibit a pure real value, following inequality should be met:

$$\frac{-\frac{g^3}{L_s^9R_L^6u^3v^3}+\frac{4bg}{L_s^6R_L^6u^2v^3}-\frac{8t}{L_s^3R_L^6uv^2}}{4\sqrt{\frac{b}{3c}+\frac{3g^2p+4sL_s^3u-12bL_s^3pu}{12L_s^6pR_L^4u^2v^2}+\frac{p}{3\cdot 2^{1/3}L_s^3R_L^4uv^2}}}+\frac{3g^2p-2sL_s^3u-6bL_s^3pu}{6L_s^6pR_L^4u^2v^2}>\frac{b}{3c}+\frac{p}{3\cdot 2^{1/3}L_s^3R_L^4uv^2} \tag{24}$$

where $s, p, z, v, u, t, g, f, e, d, c$ and b are as follows:

$$s=\left(2^{1/3}\left((b)^2+12(c)(d)-3(e)(f)\right)\right) \tag{25}$$

$$p=\left(2b^3-72bcd+27de^2-9bef+27cf^2+\sqrt{-4\left(b^2+12cd-3ef\right)^3+\left(2b^3-72bcd+27de^2-9bef+27cf^2\right)^2}\right)^{1/3} \tag{26}$$

$$z=-2L_p^2L_s^4\omega_0^2\left(-2R_L^2+L_s^2\omega_0^2\right)+M^4\left(R_L^4-2L_s^4\omega_0^4+L_s^2R_L^2\omega_0^2\left(1+C_sL_s\omega_0^2\right)\right)+L_pL_s^3M^2\omega_0^2\left(4L_s^2\omega_0^2-R_L^2\left(5+C_sL_s\omega_0^2\right)\right) \tag{27}$$

$$v=L_p-C_sM^2\omega_0^2 \tag{28}$$

$$u=L_pL_s-M^2 \tag{29}$$

$$\begin{aligned}t=&-3L_pM^4R_L^4\omega_0^4-4L_p^3L_s^4R_L^2\omega_0^6+7L_p^2L_s^3M^2R_L^2\omega_0^6-L_pL_s^2M^4R_L^2\omega_0^6-L_sM^6R_L^2\omega_0^6+C_sM^6R_L^4\omega_0^6+2L_p^3L_s^6\omega_0^8-5L_p^2L_s^5M^2\omega_0^8\\&+4L_pL_s^4M^4\omega_0^8-L_s^3M^6\omega_0^8+C_sL_p^2L_s^4M^2R_L^2\omega_0^8-2C_sL_pL_s^3M^4R_L^2\omega_0^8+C_sL_s^2M^6R_L^2\omega_0^8\end{aligned} \tag{30}$$

$$\begin{aligned}g=&-M^4R_L^4-4L_p^2L_s^4M^2R_L^2\omega_0^2+5L_pL_s^3M^2R_L^2\omega_0^2-L_s^2M^4R_L^2\omega_0^2+2L_p^2L_s^6\omega_0^4-4L_pL_s^5M^2\omega_0^4+2L_s^4M^4\omega_0^4+C_sL_pL_s^4M^2R_L^2\omega_0^4\\&-C_sL_s^3M^4R_L^2\omega_0^4\end{aligned} \tag{31}$$

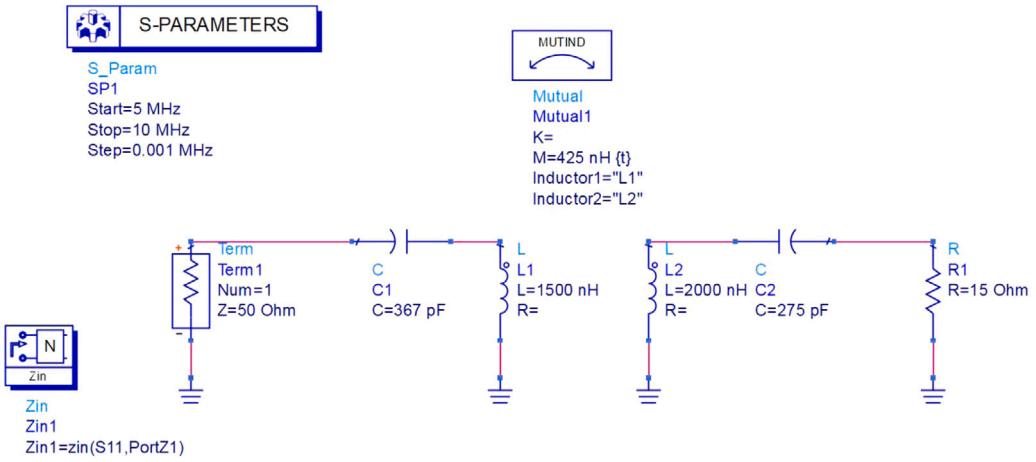

Fig. 5. A circuit simulation setup in ADS.

$$
\begin{aligned}
f = {} & -3L_pM^4R_L^6\omega_0^4 - 4L_p^3L_s^4R_L^4\omega_0^6 + 7L_p^2L_s^3M^2R_L^4\omega_0^6 - L_pL_s^2M^4R_L^4\omega_0^6 - L_sM^6R_L^4\omega_0^6 \\
& + C_sM^6R_L^6\omega_0^6 + 2L_p^3L_s^6R_L^2\omega_0^8 - 5L_p^2L_s^5M^2R_L^2\omega_0^8 \\
& + 4L_pL_s^4M^4R_L^2\omega_0^8 - L_s^3M^6R_L^2\omega_0^8 + C_sL_p^2L_s^4M^2R_L^4\omega_0^8 - 2C_sL_pL_s^3M^4R_L^4\omega_0^8 + C_sL_s^2M^6R_L^4\omega_0^8
\end{aligned} \tag{32}
$$

$$
\begin{aligned}
e = {} & -L_pM^4R_L^6 - 4L_p^3L_S^4R_L^4\omega_0^2 + 5L_p^2L_S^3M^2R_L^4\omega_0^2 - L_pL_S^2M^4R_L^4\omega_0^2 + C_SM^6R_L^6\omega_0^2 \\
& + 2L_p^3L_S^6R_L^2\omega_0^4 - 4L_p^2L_S^5M^2R_L^2\omega_0^4 + 2L_pL_S^4M^4R_L^2\omega_0^4 \\
& + 5C_sL_p^2L_S^4M^2R_L^4\omega_0^4 - 6C_sL_pL_S^3M^4R_L^4\omega_0^4 + C_sL_S^2M^6R_L^4\omega_0^4 \\
& - 2C_sL_p^2L_S^6M^2R_L^2\omega_0^6 + 4C_sL_pL_S^5M^4R_L^2\omega_0^6 \\
& - 2C_sL_S^4M^6R_L^2\omega_0^6 - C_s^2L_pL_S^4M^4R_L^4\omega_0^6 + C_s^2L_S^3M^6R_L^4\omega_0^6
\end{aligned} \tag{33}
$$

$$
d = L_pM^4R_L^6\omega_0^6 + L_p^3L_S^4R_L^4\omega_0^8 - 2L_p^2L_S^3M^2R_L^4\omega_0^6 + L_pL_S^2M^4R_L^4\omega_0^8 \tag{34}
$$

$$
c = L_p^3L_S^4R_L^4 - L_p^2L_S^3M^2R_L^4 - 2C_sL_p^2L_S^4M^2R_L^4\omega_0^2 + 2C_sL_pL_S^3M^4R_L^4\omega_0^2 + C_s^2L_pL_S^4M^4R_L^4\omega_0^4 - C_s^2L_S^3M^6R_L^4\omega_0^4 \tag{35}
$$

$$
\begin{aligned}
b = {} & 3L_pM^4R_L^4\omega_0^2 + 6L_p^3L_s^4R_L^4\omega_0^4 - 9L_p^2L_s^3M^2R_L^4\omega_0^4 + L_pL_s^2M^4R_L^4\omega_0^4 + L_sM^6R_L^4\omega_0^4 \\
& - 2C_sM^6R_L^6\omega_0^4 - 4L_p^3L_s^6R_L^2\omega_0^6 + 9L_p^2L_s^5M^2R_L^2\omega_0^6 \\
& - 6L_pL_s^4M^4R_L^2\omega_0^6 + L_s^3M^6R_L^2\omega_0^6 - 4C_sL_p^2L_s^4M^2R_L^2\omega_0^6 \\
& + 6C_sL_pL_s^3M^4R_L^4\omega_0^6 - C_sL_s^2M^6R_L^4\omega_0^6 + L_p^3L_s^8\omega_0^8 \\
& - 3L_p^2L_s^7M^2\omega_0^8 + 3L_pL_s^6M^4\omega_0^8 - L_s^5M^6\omega_0^8 + C_sL_p^2L_s^6M^2R_L^2\omega_0^8 - 2C_sL_pL_s^5M^4R_L^2\omega_0^8 + C_sL_s^4M^6R_L^2\omega_0^8
\end{aligned} \tag{36}
$$

3. Validation and discussions of solutions in Section 2

The closed-form solutions for ZPA frequencies, bifurcation conditions, and input resistances are validated using the RF circuit simulator ADS [34]. The MUTIND component in ADS, which models mutual inductance, is utilized to represent the coupled coils. Separate circuit setups are designed for each of the four compensation topologies, with three distinct sets of component values selected for each topology to simulate different operating conditions: weakly-coupled operation when the bifurcation criterion is not met, critically-coupled operation at the bifurcation point, and strongly-coupled operation when the bifurcation criterion is met. In this section, numerical results obtained from the closed-form solutions in Section 2 for these three sets of component values in each compensation scheme are compared with those derived from ADS simulations to verify the accuracy of the proposed solutions.

3.1. Validation of SS-compensation topology

The circuit schematic for the SS-compensation shown in Fig. 1 is set up in ADS as given in Fig. 5. As seen in Fig. 5, the RF port is connected instead of a high frequency voltage source seen in Fig. 1. An Sparameters simulation, in one-port configuration, is then performed in the frequency range of 6 MHz–8 MHz.

In these validation simulations the resonance frequency of the system was set to 6.786 MHz. Nonidentical primary and secondary coils with self-inductance values of $L_p = 1.5$ μH and $L_s = 2$ μH are chosen, respectively. Then, the primary side and secondary side

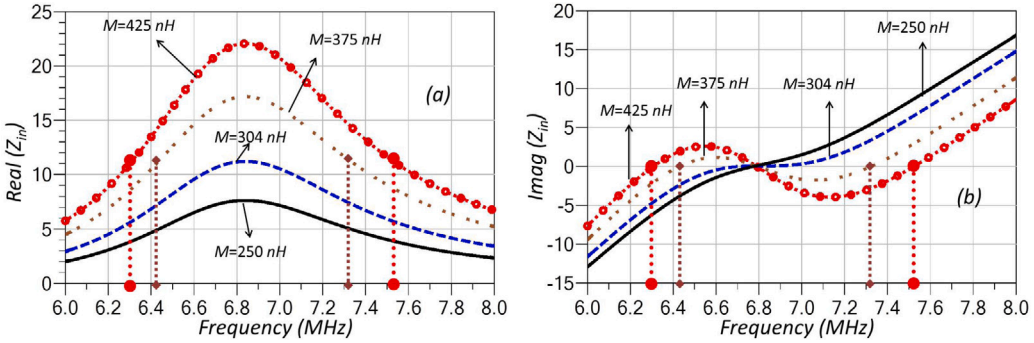

Fig. 6. SS-compensation simulation results for non-identical coils. (a) Real and (b) imaginary parts of the input impedance (Zin) obtained from ADS simulations for four different mutual inductance values: 250 nH, 303 nH, 375 nH and 425 nH.

compensation capacitors, C_p and C_s, are calculated using (4) and (5) as 367 pF and 275 pF, respectively. The load resistance R_L is set to 15 Ω. The mutual inductance value initially started from 250 nH, and then increased all the way up to 425 nH. Fig. 6 shows real and imaginary parts of the input impedance (Z_{in}) obtained from ADS simulations for four different mutual inductance values: 250 nH, 303 nH, 375 nH and 425 nH As seen in Fig. 6(b), there is only one ZPA frequency at $f_0 = 6.786$ MHz when mutual inductance value is 250 nH. When the mutual inductance is above 303 nH, which is the bifurcation point (critically coupling point), then two more ZPA frequencies, f_L and f_H, emerge resulting in a total of three ZPA frequencies (f_L, f_0 and f_H).

For SS compensation, numerical values are obtained from the closed-form solutions in Table 1, presented in Section 2, using the specified component values. Table 6 compares the numerical results for ZPA frequencies, input resistances (R_{in}), and bifurcation conditions between ADS simulations (shown in Fig. 6) and the closed-form solutions (refer to Table 1 and Eq. (7)). It is important to note that the ZPA frequencies (ω_L, ω_0 and ω_H) in Section 2 are expressed as angular frequencies in radians per second and have been converted to standard ZPA frequencies (f_L, f_0 and f_H) in hertz (Hz). The comparison demonstrates a very good agreement between the closed-form solutions and ADS simulations.

As shown in Table 6, when the mutual inductance (M) is 250 nH, the split ZPA frequencies (f_L and f_H) do not appear because the bifurcation condition in Eq. (7) is not met. This situation is known as the weakly coupled regime [12]. When M increases to 304 nH, the split frequencies still do not appear, but this is the point where both sides of the bifurcation inequality in Eq. (7) become equal, marking the bifurcation or critical coupling point [12]. For values of M greater than this, such as 375 nH and 425 nH, the bifurcation condition is satisfied, leading to the appearance of the split ZPA frequencies (f_L and f_H), as shown in Fig. 6(b) and Table 6.

The comparison of R_{in} values at ZPA frequencies also demonstrates excellent agreement between the closed-form expressions and ADS simulations. The R_{in} at f0 (6.786 MHz) increases continuously with increasing M. However, in the strongly coupled regime, R_{in} at f_L and f_H stays nearly constant as M increases. This behavior is a typical characteristic of input resistance at ZPA frequencies and is well captured by the derived closed-form expression.

Another important characteristic of the SS-compensation topology is that, when coils are identical, then the load resistance is directly reflected to the input resistance ($R_{in} = R_L$) at the split ZPA frequencies (f_L and f_H), when the system is in strongly couple regime. Here both primary and secondary side inductor values are set to 1.5 μH $\left(L_p = L_s = L = 1.5\ \mu\text{H}\right)$. The C_p and C_s, are calculated using (4) and (5) as 367 pF. Rest of the components are of the same value for the simulation results in Table 6. Fig. 7 shows the input impedance from ADS simulations for these identical coils.

Table 7 compares the numerical results for ZPA frequencies, input resistances $\left(R_{in}\right)$ at ZPA frequencies, and bifurcation conditions obtained from ADS simulations (Fig. 7) with the closed-form solutions for identical coils (Table 2). The comparison reveals a high level of agreement between the simulation results and the closed-form expressions. Notably, the R_{in} values at f_L and f_H are 15 Ω, which matches R_L $\left(R_{\text{in}} = R_L = 15\ \Omega\right)$, irrespective of the value of M, provided the system remains in the strongly coupled regime (i.e., the bifurcation criteria are satisfied). This is clearly reflected in the closed-form expressions presented in Table 2 for identical coils. This direct reflection of R_L to R_{in} at f_L and f_H has been exploited for implementing frequency-tuned coupling independent wireless power transfer systems [12–18].

3.2. Validation of SP-compensation topology

The SP-compensation topology circuit schematic, depicted in Fig. 2, is implemented in ADS as well. An S-parameter simulation is conducted in a one-port configuration over the frequency range of 5 MHz to 8 MHz. A load resistance, R_L, of 300 Ω is used, along with identical primary and secondary coils, each having a self-inductance of $L_p = L_s = 1$ μH. The secondary capacitor, C_s, is calculated to be 550 pF using Eq. (4), targeting an operating frequency of 6.786 MHz. The primary side compensation capacitor, C_p, which is highly dependent on the mutual inductance (M), is determined using Eq. (10). In practical IWPT system, this capacitor needs to. be tuned if the distance and/or alignment between coils vary during the operation. This means additional complexity needs

Table 6
Comparison between closed-form solution and ADS simulation for SS-compensation.

Parameter		Closed-form solution (based on Eq. in Table 1)	ADS simulation (see Fig. 6)
ZPA frequencies	M = 250 nH	f_L = not exists f_0 = 6.786 MHz f_H = not exists	f_L = not exists f_0 = 6.782 MHz f_H = not exists
	M = 303 nH	f_L = not exists f_0 = 6.786 MHz f_H = not exists	f_L = not exists f_0 = 6.782 MHz f_H = not exists
	M = 375 nH	f_L = 6.431 MHz f_0 = 6.786 MHz f_H = 7.322 MHz	f_L = 6.431 MHz f_0 = 6.783 MHz f_H = 7.326 MHz
	M = 425 nH	f_L = 6.306 MHz f_0 = 6.786 MHz f_H = 7.52 MHz	f_L = 6.308 MHz f_0 = 6.785 MHz f_H = 7.524 MHz
Input resistance (R_{in})	M = 250 nH M = 303 nH	R_{in} = 7.56 Ω at f_0 R_{in} = 11.12 Ω at f_0	R_{in} = 7.54 Ω at f_0 R_{in} = 11.10 Ω at f_0
	M = 375 nH	R_{in} = 11.14 Ω at f_L R_{in} = 17.02 Ω at f_0 R_{in} = 11.14 Ω at f_H	R_{in} = 11.14 Ω at f_L R_{in} = 17.00 Ω at f_0 R_{in} = 11.15 Ω at f_H
	M = 425 nH	R_{in} = 11.2 Ω at f_L R_{in} = 21.85 Ω at f_0 R_{in} = 11.2 Ω at f_H	R_{in} = 11.202 Ω at f_L R_{in} = 21.86 Ω at f_0 R_{in} = 11.26 Ω at f_H
M at bifurcation condition		304 nH	304 nH

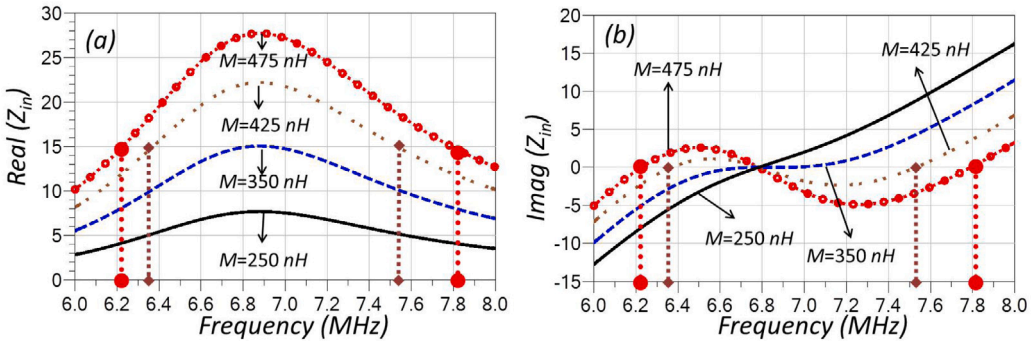

Fig. 7. SS-compensation simulation results for identical coils. (a) Real and (b) imaginary parts of the input impedance (Zin) obtained from ADS simulations for four different mutual inductance values: 250 nH, 350 nH, 425 nH and 475 nH.

to be added to the system as compared to SScompensation scheme in which C_p is just dependent on the primary side inductor, L_p as seen in (5).

The mutual inductance is initially set to 100 nH and is then incrementally increased to 300 nH. Fig. 8 illustrates the real and imaginary components of the input impedance (Z_{in}) obtained from ADS simulations for four mutual inductance values: 100 nH, 140 nH, 250 nH, and 300 nH. As seen in Fig. 8(b), there is only one ZPA frequency at $f_0 = 6.786$ MHz when mutual inductance value is 100 nH. When the mutual inductance is above 140 nH, which is the bifurcation point (critically coupling point), then two more ZPA frequencies, f_L and f_H, emerge resulting in a total of three ZPA frequencies $(f_L, f_0$ and $f_H)$.

For SP-compensation, numerical values are calculated using the closed-form solutions in Table 3 presented in Section 2 for the specified component values. Table 8 provides a comparison of the numerical results for ZPA frequencies, input resistances (R_{in}), and bifurcation conditions between ADS simulations (see Fig. 8) and the closed-form solutions (refer to Table 3). A very good agreement is obtained between the closed form solutions and ADS simulations for the SP-compensation as well. It should be noted that the coils here in these simulations for SP-compensation validations are chosen identical for simplicity; however, the closed-form expressions in Table 3 works perfectly for non-identical coils, different component values and design frequencies.

3.3. Validation of PS-compensation topology

The PS-compensation topology circuit schematic, depicted in Fig. 3, is implemented in ADS. An Sparameter simulation is conducted in a one-port configuration over the frequency range of 6 MHz to 8 MHz. A load resistance, R_L, of 5 Ω is used, along with identical primary and secondary coils, each having a self-inductance of $L_p = L_s = 1$ μH. The secondary capacitor, C_s, is calculated to be 550 pF using Eq. (4), targeting an operating frequency of 6.786 MHz. The primary side compensation capacitor, which is highly

Table 7
Comparison between closed-form solution and ADS simulation for SS-compensation (Identical coils).

Parameter		Closed-form solution (Table 2)	ADS simulation (Fig. 7)
ZPA frequencies	$M = 250$ nH	f_L = not exists $f_0 = 6.786$ MHz f_H = not exists	f_L = not exists $f_0 = 6.784$ MHz f_H = not exists
	$M = 350$ nH	f_L = not exists $f_0 = 6.786$ MHz f_H = not exists	f_L = not exists $f_0 = 6.783$ MHz f_H = not exists
	$M = 425$ nH	$f_L = 6.371$ MHz $f_0 = 6.786$ MHz $f_H = 7.530$ MHz	$f_L = 6.371$ MHz $f_0 = 6.785$ MHz $f_H = 7.531$ MHz
	$M = 475$ nH	$f_L = 6.224$ MHz $f_0 = 6.786$ MHz $f_H = 7.790$ MHz	$f_L = 6.226$ MHz $f_0 = 6.786$ MHz $f_H = 7.791$ MHz
Input resistance (R_{in})	$M = 250$ nH $M = 350$ nH	$R_{\text{in}} = 7.55\ \Omega$ at f_0 $R_{\text{in}} = 14.98\ \Omega$ at f_0	$R_{\text{in}} = 7.55\ \Omega$ at f_0 $R_{\text{in}} = 14.87\ \Omega$ at f_0
	$M = 425$ nH	$R_{\text{in}} = 15\ \Omega$ at f_L $R_{\text{in}} = 21.859\ \Omega$ at f_0 $R_{\text{in}} = 15\ \Omega$ at f_H	$R_{\text{in}} = 15\ \Omega$ at f_L $R_{\text{in}} = 21.9\ \Omega$ at f_0 $R_{\text{in}} = 15\ \Omega$ at f_H
	$M = 475$ nH	$R_{\text{in}} = 14.99\ \Omega$ at f_L $R_{\text{in}} = 27.3\ \Omega$ at f_0 $R_{\text{in}} = 15\ \Omega$ at f_H	$R_{\text{in}} = 15\ \Omega$ at f_L $R_{\text{in}} = 27.305\ \Omega$ at f_0 $R_{\text{in}} = 15\ \Omega$ at f_H
M at bifurcation condition		350 nH	350 nH

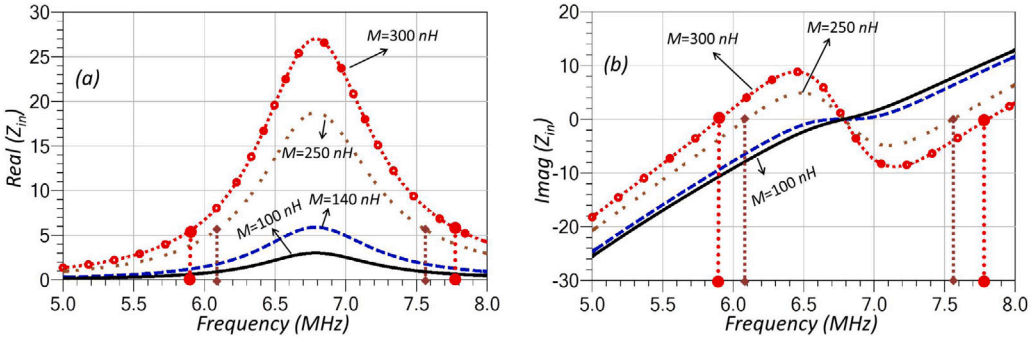

Fig. 8. SP-compensation simulation results. (a) Real and (b) imaginary parts of the input impedance (Zin) obtained from ADS simulations for four different mutual inductance values: 100 nH, 140 nH, 250 nH and 300 nH.

Table 8
Comparison between closed-form solution and ADS simulation for SP-compensation.

Parameter		Closed-form solution (based on Eq. in Table 3)	ADS simulation (see Fig. 8)
ZPA frequencies	$M = 100$ nH	f_L = not exists $f_0 = 6.786$ MHz f_H = not exists	f_L = not exists $f_0 = 6.786$ MHz f_H = not exists
	$M = 140$ nH	f_L = not exists $f_0 = 6.786$ MHz f_H = not exists	f_L = not exists $f_0 = 6.785$ MHz f_H = not exists
	$M = 250$ nH	$f_L = 6.095$ MHz $f_0 = 6.786$ MHz $f_H = 7.556$ MHz	$f_L = 6.094$ MHz $f_0 = 6.786$ MHz $f_H = 7.557$ MHz
	$M = 300$ nH	$f_L = 5.9$ MHz $f_0 = 6.786$ MHz $f_H = 7.8$ MHz	$f_L = 5.901$ MHz $f_0 = 6.786$ MHz $f_H = 7.805$ MHz
Input resistance (R_{in})	$M = 100$ nH $M = 140$ nH	$R_{\text{in}} = 3\ \Omega$ at f_0 $R_{\text{in}} = 5.88\ \Omega$ at f_0	$R_{\text{in}} = 3\ \Omega$ at f_0 $R_{\text{in}} = 5.88\ \Omega$ at f_0
	$M = 250$ nH	$R_{\text{in}} = 5.65\ \Omega$ at f_L $R_{\text{in}} = 18.75\ \Omega$ at f_0 $R_{\text{in}} = 5.66\ \Omega$ at f_H	$R_{\text{in}} = 5.678\ \Omega$ at f_L $R_{\text{in}} = 18.753\ \Omega$ at f_0 $R_{\text{in}} = 5.683\ \Omega$ at f_H
	$M = 300$ nH	$R_{\text{in}} = 5.49\ \Omega$ at f_L $R_{\text{in}} = 27\ \Omega$ at f_0 $R_{\text{in}} = 5.54\ \Omega$ at f_H	$R_{\text{in}} = 5.516\ \Omega$ at f_L $R_{\text{in}} = 27\ \Omega$ at f_0 $R_{\text{in}} = 5.52\ \Omega$ at f_H
M at bifurcation condition		140 nH	140 nH

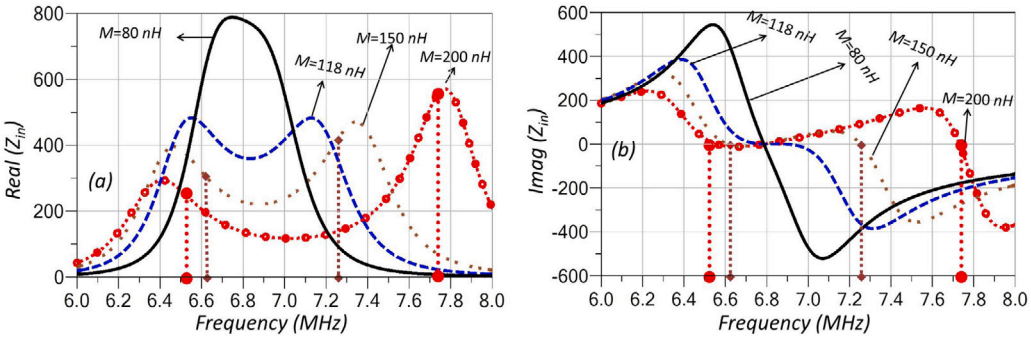

Fig. 9. PS-compensation simulation results. (a) Real and (b) imaginary parts of the input impedance (Zin) obtained from ADS simulations for four different mutual inductance values: 80 nH, 118 nH, 150 nH and 200 nH.

Table 9
Comparison between closed-form solution and ADS simulation for PS-compensation.

Parameter		Closed-form solution (based on Eq. in Table 4)	ADS simulation (see Fig. 9)
ZPA frequencies	M = 80 nH	f_L = not exists f_0 = 6.786 MHz f_H = not exists	f_L = not exists f_0 = 6.786 MHz f_H = not exists
	M = 118 nH	f_L = not exists f_0 = 6.786 MHz f_H = not exists	f_L = not exists f_0 = 6.785 MHz f_H = not exists
	M = 150 nH	f_L = 6.612 MHz f_0 = 6.786 MHz f_H = 7.255 MHz	f_L = 6.611 MHz f_0 = 6.786 MHz f_H = 7.255 MHz
	M = 200 nH	f_L = 6.555 MHz f_0 = 6.786 MHz f_H = 7.733 MHz	f_L = 6.556 MHz f_0 = 6.786 MHz f_H = 7.73 MHz
Input resistance (R_{in})	M = 80 nH	R_{in} = 783.57 Ω at f_0	R_{in} = 783.33 Ω at f_0
	M = 118 nH	R_{in} = 364.15 Ω at f_0	R_{in} = 363.95 Ω at f_0
	M = 150 nH	R_{in} = 310.23 Ω at f_L R_{in} = 230.4 Ω at f_0 R_{in} = 416.4 Ω at f_H	R_{in} = 310.34 Ω at f_L R_{in} = 230.17 Ω at f_0 R_{in} = 416.8 Ω at f_H
	M = 200 nH	R_{in} = 230.8 Ω at f_L R_{in} = 139.54 Ω at f_0 R_{in} = 549.9 Ω at f_H	R_{in} = 230.8 Ω at f_L R_{in} = 139.52 Ω at f_0 R_{in} = 550 Ω at f_H
M at bifurcation condition		118 nH	118 nH

dependent on the mutual inductance (M), and load, R_L, is determined using Eq. (10). In practical IWPT system, this capacitor needs to be tuned not only with the distance and/or alignment between coils but also the varying load conditions such as state of charge and battery capacity. This means even further complexity needs to be added to the system as compared to SP-compensation topology.

In ADS simulations the mutual inductance is initially set to 80 nH and is then incrementally increased to 200 nH. Fig. 9 illustrates the real and imaginary components of the input impedance (Z_{in}) obtained from ADS simulations for four mutual inductance values: 80 nH, 118 nH, 150 nH, and 200 nH. As seen in Fig. 9(b), the input impedance is inductive at low frequencies, which is opposite to the behavior of SS and SP topologies where input impedance is capacitive at the low frequency range. There is only one ZPA frequency at $f_0 = 6.786$ MHz when mutual inductance value is 80 nH. When the mutual inductance is above 118 nH, which is the bifurcation point (critically coupling point), then two more ZPA frequencies, f_L and f_H, emerge resulting in a total of three ZPA frequencies $(f_L, f_0$ and $f_H)$.

For PS-compensation, numerical values are calculated using the closed-form solutions in Table 4 presented in Section 2 for the specified component values. Table 9 provides a comparison of the numerical results for ZPA frequencies, input resistances (R_{in}), and bifurcation conditions between ADS simulations (see Fig. 9) and the closed-form solutions (refer to Table 4). A very good agreement is obtained between the closed form solutions and ADS simulations for the PS-compensation as well. It should be noted that the coils here in these simulations for PS-compensation validations also are chosen identical for simplicity; however, the closed-form expressions in Table 4 works perfectly for non-identical coils, different component values and design frequencies.

3.4. Validation of PP-compensation topology

The PP-compensation topology circuit schematic, depicted in Fig. 4, is implemented in ADS. In PPcompensation simulations, the higher split ZPA frequency (f_H) varies in wider frequency range, therefore, simulations were also performed in a wider frequency range. An S-parameter simulation is conducted in a one-port configuration over the frequency range of 3 MHz to 20 MHz. A load resistance, R_L, of 75.26 Ω is used, along with identical primary and secondary coils, each having a self-inductance of $L_p = L_s = 310$ nH. The secondary capacitor, C_s, is calculated to be $1.774nF$ using Eq. (4), targeting an operating frequency of 6.786 MHz. The primary side compensation capacitor, which is highly dependent on the mutual inductance (M) and R_L, is determined

Table 10
Comparison between closed-form solution and ADS simulation for PP-compensation.

Parameter		Closed-form solution (based on Eq. in Table 5)	ADS Simulation (see Fig. 10)
ZPA frequencies	$M = 38$ nH	f_L = not exists $f_0 = 6.786$ MHz f_H = not exists	f_L = not exists $f_0 = 6.786$ MHz f_H = not exists
	$M = 52$ nH	f_L = not exists $f_0 = 6.786$ MHz f_H = not exists	f_L = not exists $f_0 = 6.785$ MHz f_H = not exists
	$M = 100$ nH	$f_L = 6.614$ MHz $f_0 = 6.786$ MHz $f_H = 8.819$ MHz	$f_L = 6.614$ MHz $f_0 = 6.786$ MHz $f_H = 8.820$ MHz
	$M = 120$ nH	$f_L = 6.869$ MHz $f_0 = 6.786$ MHz $f_H = 10.302$ MHz	$f_L = 6.870$ MHz $f_0 = 6.786$ MHz $f_H = 10.30$ MHz
	$M = 150$ nH	$f_L = 7.404$ MHz $f_0 = 6.786$ MHz $f_H = 14.27$ MHz	$f_L = 7.403$ MHz $f_0 = 6.786$ MHz $f_H = 14.27$ MHz
Input resistance (R_{in})	$M = 38$ nH	$R_{\text{in}} = 151.1\ \Omega$ at f_0	$R_{\text{in}} = 151\ \Omega$ at f_0
	$M = 52$ nH	$R_{\text{in}} = 80.04\ \Omega$ at f_0	$R_{\text{in}} = 80.04\ \Omega$ at f_0
	$M = 100$ nH	$R_{\text{in}} = 33.04\ \Omega$ at f_L $R_{\text{in}} = 25.8\ \Omega$ at f_0 $R_{\text{in}} = 220.6\ \Omega$ at f_H	$R_{\text{in}} = 33.04\ \Omega$ at f_L $R_{\text{in}} = 25.8\ \Omega$ at f_0 $R_{\text{in}} = 220.6\ \Omega$ at f_H
	$M = 120$ nH	$R_{\text{in}} = 19.817\ \Omega$ at f_L $R_{\text{in}} = 22.47\ \Omega$ at f_0 $R_{\text{in}} = 487.7\ \Omega$ at f_H	$R_{\text{in}} = 19.82\ \Omega$ at f_L $R_{\text{in}} = 22.47\ \Omega$ at f_0 $R_{\text{in}} = 487.7\ \Omega$ at f_H
	$M = 150$ nH	$R_{\text{in}} = 9.427\ \Omega$ at f_L $R_{\text{in}} = 23.43\ \Omega$ at f_0 $R_{\text{in}} = 1855\ \Omega$ at f_H	$R_{\text{in}} = 9.43\ \Omega$ at f_L $R_{\text{in}} = 23.43\ \Omega$ at f_0 $R_{\text{in}} = 1855\ \Omega$ at f_H
M at bifurcation condition		52 nH	52 nH

using Eq. (19). As in PS-compensation topology, this capacitor needs to be tuned with both the distance and/or alignment between coils and varying load conditions.

In ADS simulations, the mutual inductance is initially set to 38 nH and gradually increased to 150 nH. Fig. 10 displays the real and imaginary components of the input impedance (Z_{in}) obtained from ADS simulations for five different mutual inductance values: 38 nH, 52 nH, 80 nH, 120 nH, and 150 nH. To clearly differentiate the simulation data for each mutual inductance value in the PP-compensation topology, separate impedance graphs are plotted for each M (see Fig. 10). As seen in Fig. 10, the input impedance is inductive at low frequencies, which is opposite to the behavior of SS and SP topologies where input impedance is capacitive at the low frequency range. There is only one ZPA frequency at $f_0 = 6.786$ MHz when M value is 38 nH. When the mutual inductance, M, exceeds 52 nH, which corresponds to the bifurcation point (critical coupling point), two additional ZPA frequencies, f_L and f_H, appear, resulting in a total of three ZPA frequencies: f_L, f_0 and f_H. These frequencies are represented by triangular markers in Fig. 10. When M reaches 100 nH and 120 nH, two of the ZPA frequencies are very close to each other, causing their markers to appear almost overlapped (see Fig. 10(c) and (d)).

For PP-compensation, numerical values are obtained from the closed-form solutions in Table 5 presented in Section 2 for the specified component values. Table 10 provides a comparison of the numerical results for ZPA frequencies and bifurcation conditions between ADS simulations (see Fig. 10) and the closed-form solutions (refer to Table 5). A very good agreement is obtained between the closed form solutions and ADS simulations for the PP-compensation as well. It should be noted that the coils here in these simulations for PS-compensation validations also are chosen identical for simplicity; however, the closed-form expressions in Table 5 works perfectly for non-identical coils, different component values and design frequencies.

A key observation from the PP-compensation simulation results is that the behavior of the split ZPA frequencies changes differently as the mutual inductance (M) increases. In SS, SP, and PS compensation simulations, when the bifurcation criterion is met, the split ZPA frequencies, f_L and f_{H2} appear below and above f_0, respectively. However, in the PP-compensation topology, once the bifurcation criterion is satisfied and M exceeds a certain threshold, both f_L and f_H emerge above f_0. This trend is clearly illustrated in Fig. 10 and Table 10. Specifically, when M is 100 nH, f_L is 6.614 MHz, which is lower than f_0(6.786 MHz). In contrast, for M values of 120 nH and 150 nH, f_L shifts to 6.869 MHz and 7.404 MHz, respectively, both of which are higher than f_0(6.786 MHz).

4. Conclusion

This paper effectively addresses significant gaps in the mathematical analysis of bifurcation phenomena in inductive wireless power transfer (IWPT) systems. The derived closed-form expressions for ZPA frequencies, input resistances, and bifurcation criteria can be readily applied to various control algorithms used in wireless power transfer systems and other inductively coupled systems. For instance, the ZPA solutions presented in this paper can be integrated into the control algorithms of frequency tracking controllers, particularly for operating the system at conditionally existing ZPA frequencies. Likewise, the derived input impedances at the ZPA frequencies can be utilized to accurately calculate the input current at these frequencies. The accuracy of the derived formulas was validated through simulation, confirming their practical applicability. Future research could extend the analysis to other compensation topologies, driving improvements in the efficiency and optimization of IWPT systems.

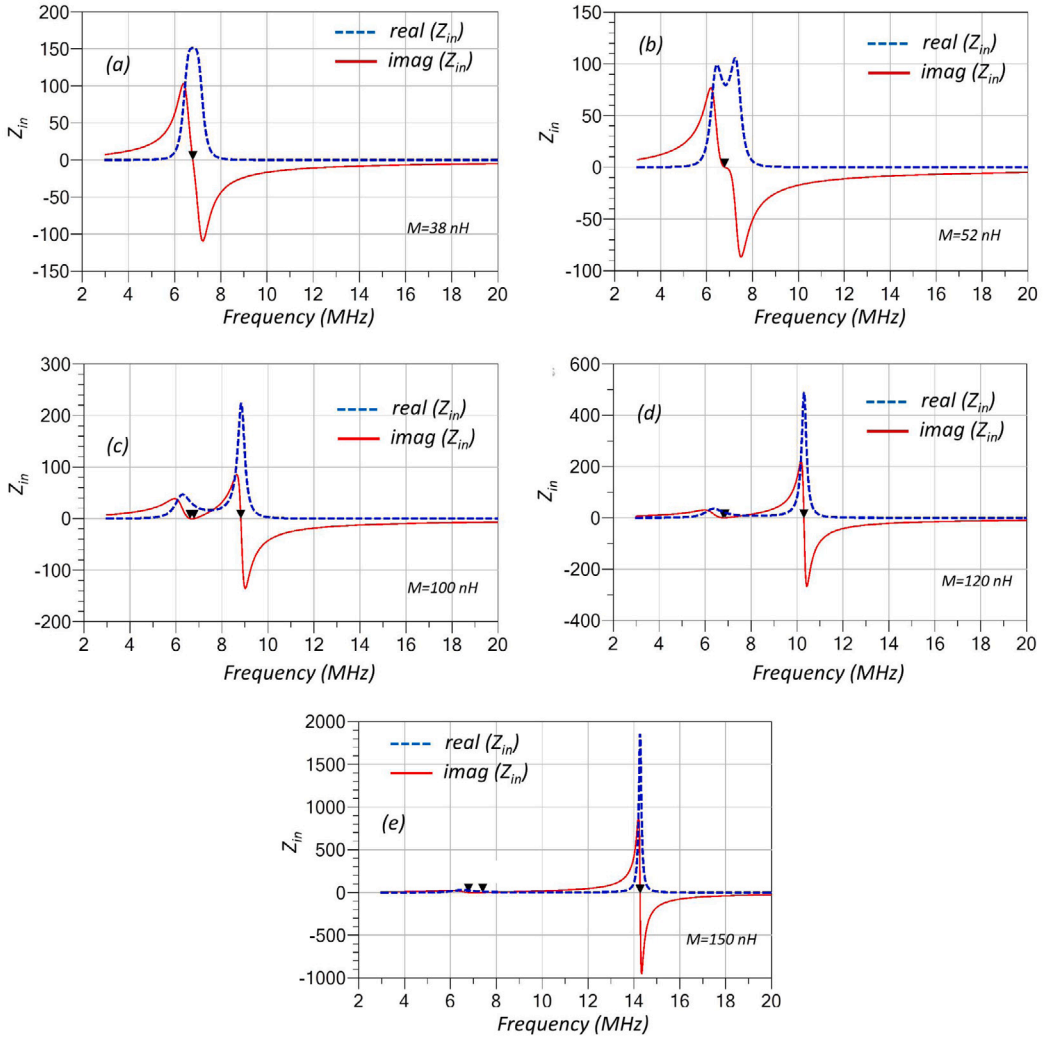

Fig. 10. PP-compensation simulation results. (a) Real and (b) imaginary parts of the input impedance (Zin) obtained from ADS simulations for four different mutual inductance values: 38 nH, 52 nH, 100 nH, 120 nH and 150 nH.

Data availability

No data was used for the research described in the article.

References

[1] Z. Zhang, H. Pang, A. Georgiadis, C. Cecati, Wireless power transfer—An overview, IEEE Trans. Ind. Electron. 66 (2) (2019) 1044–1058, http://dx.doi.org/10.1109/TIE.2018.2835378.

[2] Q. Wang, W. Che, M. Mongiardo, G. Monti, Wireless power transfer system with high misalignment tolerance for bio-medical implants, IEEE Trans. Circuits Syst. II Express Briefs 67 (12) (2020) 3023–3027, http://dx.doi.org/10.1109/TCSII.2020.2985056.

[3] J. Lu, G. Zhu, D. Lin, Y. Zhang, H. Wang, C.C. Mi, Realizing constant current and constant voltage outputs and input zero phase angle of wireless power transfer systems with minimum component counts, IEEE Trans. Intell. Transp. Syst. 22 (1) (2021) 600–610, http://dx.doi.org/10.1109/TITS.2020.2985658.

[4] W. Zhang, C.C. Mi, Compensation topologies of high-power wireless power transfer systems, IEEE Trans. Veh. Technol. 65 (6) (2016) 4768–4778, http://dx.doi.org/10.1109/TVT.2015.2454292.

[5] V. Shevchenko, O. Husev, R. Strzelecki, B. Pakhaliuk, N. Poliakov, N. Strzelecka, Compensation topologies in IPT systems: Standards, requirements, classification, analysis, comparison and application, IEEE Access 7 (2019) 120559–120580, http://dx.doi.org/10.1109/ACCESS.2019.2937891.

[6] M. Abou Houran, X. Yang, W. Chen, Magnetically coupled resonance WPT: Review of compensation topologies, resonator structures with misalignment, and EMI diagnostics, Electronics 7 (11) (2018) 296.

[7] C.-S. Wang, G.A. Covic, O.H. Stielau, Power transfer capability and bifurcation phenomena of loosely coupled inductive power transfer systems, IEEE Trans. Ind. Electron. 51 (1) (2004) 148–157, http://dx.doi.org/10.1109/TIE.2003.822038.

[8] E.R. Joy, B.K. Kushwaha, G. Rituraj, P. Kumar, Analysis and comparison of four compensation topologies of contactless power transfer system, in: Proc. 2015 4th Int. Conf. Electr. Power Energy Convers. Syst. (EPECS), Sharjah, UAE, 2015, pp. 1–6, http://dx.doi.org/10.1109/EPECS.2015.7368544.
[9] B. Alam, N. Islam, I. Subhan, M. Sarfraz, Analysis and modelling of basic wireless power transfer compensation topology: A review, Intell. Data Anal. Power Energy Syst. (2022) 501–515.
[10] D.B. Ahire, V.J. Gond, J.J. Chopade, Compensation topologies for wireless power transmission system in medical implant applications: A review, Biosens. Bioelectron. X 11 (2022) 100180.
[11] S.O. Ozkilic, A. Agcal, K. Toraman, Comparison of compensating topologies in two coil resonant wireless power transfer system, J. Eng. Res. 11 (2B) (2023).
[12] S.A. Sis, S. Bicakci, A resonance frequency tracker and source frequency tuner for inductively coupled wireless power transfer systems, in: Proc. 2016 46th Eur. Microw. Conf. (EuMC), London, UK, 2016, pp. 751–754, http://dx.doi.org/10.1109/EuMC.2016.7824452.
[13] D.-W. Seo, J.-H. Lee, Frequency-tuning method using the reflection coefficient in a wireless power transfer system, IEEE Microw. Wirel. Compon. Lett. 27 (11) (2017) 959–961, http://dx.doi.org/10.1109/LMWC.2017.2750023.
[14] F. Kilic, S. Sezen, S.A. Sis, A misalignment-adaptive wireless power transfer system using PSO-based frequency tracking, Int. J. Optim. Control.: Theor. Appl. (IJOCTA) 10 (2) (2020) 206–217.
[15] Y. Liu, F. Liu, H. Feng, G. Zhang, L. Wang, R. Chi, K. Li, Frequency tracking control of the WPT system based on fuzzy RBF neural network, Int. J. Intell. Syst. 37 (7) (2022) 3881–3899.
[16] J. Hu, J. Zhao, Y. Yang, W. Zhong, Low-frequency pulse control for self-oscillation-based resonance tracking of wireless power transfer systems, IEEE Trans. Ind. Electron. 71 (9) (2024) 10591–10600, http://dx.doi.org/10.1109/TIE.2023.3342284.
[17] J. Xia, D. Wang, D. Xu, A hybrid frequency adjusting method for the wireless power transfer system, Electr. Eng. 104 (4) (2022) 2679–2688.
[18] Y. Zhang, T. Kan, Z. Yan, C.C. Mi, Frequency and voltage tuning of series–series compensated wireless power transfer system to sustain rated power under various conditions, IEEE J. Emerg. Sel. Top. Power Electron. 7 (2) (2019) 1311–1317, http://dx.doi.org/10.1109/JESTPE.2018.2871636.
[19] F.N. Esfahani, S.M. Madani, M. Niroomand, A. Safaee, Maximum wireless power transmission using real-time single iteration adaptive impedance matching, IEEE Trans. Circuits Syst. I. Regul. Pap. 70 (9) (2023) 3806–3817, http://dx.doi.org/10.1109/TCSI.2023.3284218.
[20] X. Zhang, J. Lu, J. Chen, L. Tong, Y. Shi, H. Qiu, Impedance matching through a reconfigurable relay coil achieving maximum wireless power transfer under variations of coupling coefficient and load resistance, IEEE Trans. Circuits Syst. I. Regul. Pap. (2024) http://dx.doi.org/10.1109/TCSI.2024.3433394.
[21] X. Li, D. Zhou, S. Jia, X. Liu, J. Zou, A WPT system with wide-range voltage gains and soft switching via primary-side hybrid modulation, IEEE Trans. Power Electron. 39 (7) (2024) 8985–8997, http://dx.doi.org/10.1109/TPEL.2024.3385391.
[22] O. Abdelatty, X. Wang, A. Mortazawi, Position-insensitive wireless power transfer based on nonlinear resonant circuits, IEEE Trans. Microw. Theory Tech. 67 (9) (2019) 3844–3855.
[23] R. Chai, A. Mortazawi, A position-insensitive wireless power transfer system employing coupled nonlinear resonators, IEEE Trans. Microw. Theory Tech. 69 (3) (2021) 1752–1759.
[24] X. Wang, O. Abdelatty, A. Mortazawi, A novel coupling factor independent highly efficient resonant based wireless power transfer, in: Proc. 2017 47th Eur. Microw. Conf. (EuMC), 2017, pp. 200–203.
[25] E.M. Thomas, J.D. Heebl, C. Pfeiffer, A. Grbic, A power link study of wireless non-radiative power transfer systems using resonant shielded loops, IEEE Trans. Circuits Syst. I. Regul. Pap. 59 (9) (2012) 2125–2136, http://dx.doi.org/10.1109/TCSI.2012.2185295.
[26] J.D. Heebl, E.M. Thomas, R.P. Penno, A. Grbic, Comprehensive analysis and measurement of frequency-tuned and impedance-tuned wireless non-radiative power-transfer systems, IEEE Antennas Propag. Mag. 56 (4) (2014) 44–60, http://dx.doi.org/10.1109/MAP.2014.6931657.
[27] L. Jianyu, T. Houjun, G. Xin, Frequency splitting analysis of wireless power transfer system based on T-type transformer model, Elektron. Elektrotech. 19 (10) (2013) 109–113.
[28] K. Aditya, S.S. Williamson, Design guidelines to avoid bifurcation in a series–series compensated inductive power transfer system, IEEE Trans. Ind. Electron. 66 (5) (2019) 3973–3982, http://dx.doi.org/10.1109/TIE.2018.2851953.
[29] W.-Q. Niu, J.-X. Chu, W. Gu, A.-D. Shen, Exact analysis of frequency splitting phenomena of contactless power transfer systems, IEEE Trans. Circuits Syst. I. Regul. Pap. 60 (6) (2013) 1670–1677, http://dx.doi.org/10.1109/TCSI.2012.2221172.
[30] M. Košík, R. Fajtl, J. Lettl, Analysis of bifurcation in two-coil inductive power transfer, in: Proc. 2017 IEEE 18th Workshop Control Model. Power Electron. (COMPEL), Stanford, CA, USA, 2017, pp. 1–8, http://dx.doi.org/10.1109/COMPEL.2017.8013324.
[31] M. Iordache, D. Niculae, L.I. Bobaru, L. Mandache, Circuit analysis of frequency splitting phenomena in wireless power transfer systems, in: Proc. 2015 9th Int. Symp. Adv. Top. Electr. Eng. (ATEE), Bucharest, Romania, 2015, pp. 146–151, http://dx.doi.org/10.1109/ATEE.2015.7133758.
[32] N. Hatchavanich, A. Sangswang, M. Konghirun, The bifurcated detection using the sensing coil for parallel-parallel compensation in IPT system, in: Proc. IECON 2020 46th Annu. Conf. IEEE Ind. Electron. Soc. Singapore, 2020, pp. 5268–5272, http://dx.doi.org/10.1109/IECON43393.2020.9254747.
[33] J. Zhou, C.Q. Jiang, T. Ma, G. Guidi, X. Zhang, J.A. Suul, Comprehensive analysis of bifurcation and frequency splitting phenomena in inductive battery charging systems, IEEE Trans. Power Electron. 39 (11) (2024) 15329–15341, http://dx.doi.org/10.1109/TPEL.2024.3434620.
[34] Agilent Advanced Design System (ADS), Ver. 2014, Agilent Technologies, Santa Rosa, CA, 2014.